Research in Astronomy and Astrophysics, 25:065009 (10pp), 2025 June
https://doi.org/10.1088/1674-4527/add3a4
CSTR: 32081.14.RAA.add3a4

Suzaku Observation of Merging Clusters A222 and A223

Yanling Chen[1], Wei Cui[1], Aurora Simionescu[2], Rui Huang[1,3], and Dan Hu[4]
[1] Department of Astronomy, Tsinghua University, Beijing 100084, China; yl-chen19@mails.tsinghua.edu.cn
[2] SRON Netherlands Institute for Space Research, Niels Bohrweg 4, 2333 CA Leiden, The Netherlands
[3] Department of Astronomy, University of Michigan, Ann Arbor, MI 48109-1107, USA
[4] Department of Theoretical Physics and Astrophysics, Faculty of Science, Masaryk University, Kotlářská 2, Brno, 611 37, Czech Republic
Received 2025 January 18; revised 2025 April 21; accepted 2025 April 29; published 2025 June 3

Abstract

Previous X-ray and optical studies of the galaxy cluster pair A222/223 suggested the possible presence of a filamentary structure connecting the two clusters, a result that appears to be supported by subsequent weak-lensing analyses. This filament has been reported to host a primordial warm-hot intergalactic medium, which existed prior to being heated by the interactions of the clusters. In this study, we made an attempt to examine the reported emission feature with data from an archival Suzaku observation, taking advantage of its low detector background. Because the emission is expected to be very weak, we first carefully examined all potential sources of "contamination," and then modeled the residual emission. Due to large uncertainties, unfortunately, our results can neither confirm the presence of the reported emission feature nor rule it out. We discuss the sources of uncertainties.

Key words: galaxies: clusters: intracluster medium – X-rays: galaxies: clusters – (cosmology:) large-scale structure of universe

1. Introduction

The cosmic missing baryon problem refers to the discrepancy between the observed baryon content in the local universe and the measurements made with the observations of the Cosmic Microwave Background, primordial elemental abundances and the Lyα forest (Cen & Ostriker 1999). Cosmological simulations (e.g., Cen & Ostriker 1999; Tuominen et al. 2021) show that the "missing" baryons are predominantly located in large-scale filamentary structures. Such diffuse gas is often referred to as warm-hot intergalactic medium (WHIM), because it is of temperature ranging from 10^5 to 10^7 K (Davé et al. 2001). Much progress has been made on detecting the warm component of WHIM with O VI absorption line observations (Shull et al. 2012). However, the hot component of WHIM is still poorly measured.

The detection of the hot component of WHIM is highly challenging in the soft X-ray band (Cen & Fang 2006). Nevertheless, extensive effort has been made to carry out absorption line observations of WHIM with X-ray gratings onboard Chandra and XMM-Newton, and positive detections have been reported (see Fang et al. 2024 for a review), albeit limited to only a few lines of sight. Attempts have also been made to detect X-ray emission from hot WHIM in a filament that connects a pair of clusters, with some success (Werner et al. 2008; Sato et al. 2010; Alvarez et al. 2018; Reiprich et al. 2021; Mirakhor et al. 2022). The A222/223 system is of particular interest in this regard. The X-ray emission from the filament connecting the two clusters was reported (Werner et al. 2008), based on XMM-Newton observations of the system, and the detection significance was said to reach about 5σ. The presence of the filament was supported by a weak lensing study, with the significance of the detection also exceeding 5σ (Dietrich et al. 2012). Neither of the two member clusters seems to be relaxed, suggesting that interaction such as merging or sloshing is taking place in the system (Durret et al. 2010).

In this work, we analyzed archival data from the Suzaku observations of A222/223, making use of its low particle background to further examine the filament emission. The structure of this paper is as follows: In Section 2 we describe the Suzaku observations and data analysis. In Section 3, we present constraints on the properties of any WHIM emission from the Suzaku data analysis. In Section 4, we discuss our findings and compare them with previous studies. Unless otherwise stated, all errors throughout this paper are quoted at the 1σ confidence level. The cosmological model adopted in this work is the standard ΛCDM cosmology, with $H_0 = 70\,\mathrm{km\,s^{-1}\,Mpc^{-1}}$, $\Omega_M = 0.3$, and $\Omega_\Lambda = 0.7$. In this framework, the angular scale is $3.427''$ per 1 kpc, calculated at the redshift of 0.21, corresponding to the A222/223 system. The quantities r_{200c} and r_{500c} represent the radii in which the mean enclosed density is 200 and 500 times the critical density of the universe, respectively.

2. Data Analysis

2.1. Suzaku Observations

A222/223 was observed by the Suzaku telescope on 2010 December 25, as shown in Table 1, along with the Chandra and XMM-Newton observations. Figure 1 presents the Suzaku view

Table 1
X-ray Observations of A222/223

Telescope	Date	ObsID	Instrument	Exposure Time (ks)
Suzaku	2010-12-25	805035010	XIS0/1/3	101
XMM-Newton	2007-06-18	0502020101 / 201	EPIC	144
Chandra	2004-09-10 / 2007-07-27	4967 / 7705	ACIS-I	50

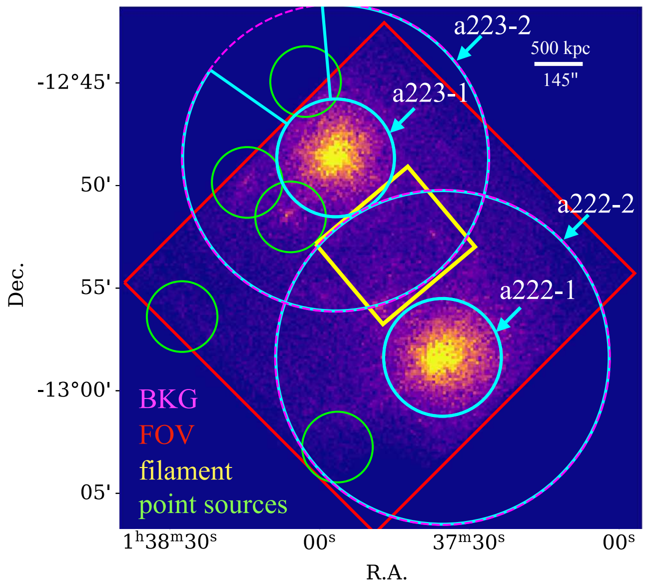

Figure 1. The 0.5–7.0 keV vignetting-corrected Suzaku image of the A222/223 galaxy cluster pair. The cyan sectors and yellow box are the spectrum extraction regions for the clusters and the filament, respectively. The magenta dashed circles represent $1.1r_{200c}$ of the two clusters, while the region outside the magenta circles is defined as the background region. The green circles mark the exclusion regions for point sources in the Suzaku data. The red box is the Suzaku FOV. The image was binned by 8 pixels, and then smoothed using a 12.5" Gaussian kernel.

of the pair of A222/223 clusters, where A223 is in the northeast and A222 is in the southwest, with their X-ray peaks at coordinates (R.A., decl.) of (01:37:33.5, −12:59:20.9) and (01:37:55.9, −12:49:21.2), respectively. The virial masses M_{200c} of the two clusters, as derived from weak lensing analysis, are determined to be $M_{200c}(\mathrm{A222}) = (2.7^{+0.8}_{-0.7}) \times 10^{14} M_\odot$ and $M_{200c}(\mathrm{A223}) = (3.4^{+1.3}_{-1.0}) \times 10^{14} M_\odot$ (Dietrich et al. 2012). To assess excess emission in the filament region, we carefully selected regions to quantify the contribution from known sources, as shown in Table 2. We defined sector regions for cluster emission, centered on the X-ray surface brightness peaks, with a222-1 and a223-1 representing the core regions and a222-2 and a223-2 the outskirts (shown in cyan). Sector radii were chosen to be sufficiently large to account for scattered cluster emission. The outer boundaries of both cluster regions extend to $1.1r_{200c}$, where r_{200c} are 1.28 ± 0.11 Mpc and 1.55 ± 0.15 Mpc for A222 and A223, respectively. Here, we defined the filament region (fila-box) as a $6'.1 \times 5'.3$ rectangular box positioned on the merging axis connecting the two clusters (marked in yellow), fully encompassed by the outer boundaries of the cluster outskirt regions. This configuration allows an assessment of the contribution of the cluster outskirts emission to the filament region. To avoid double accounting, we carefully separated the filament, a222-2, and a223-2 regions in their definitions. A sky background region (bkg) was defined as the area outside the magenta circles marking the $1.1r_{200c}$ boundaries of both clusters. The point sources with 2–8 keV flux exceeding 1.8×10^{-14} erg s^{-1} cm^{-2} are marked in green circles and are removed from subsequent analyses. For Suzaku data pre-reduction, we generally followed the official pipeline of the X-ray Imaging Spectrometers (XIS).[5] We used the standard screened event files from the observation and combined events from both the 5 × 5 and 3 × 3 clocking modes. The cutoff rigidity (COR) was set to a threshold of 8 GV instead of 6 GV. After the screening, we examined the light curves of the observations and excluded the time intervals with a count rate exceeding 3σ, which returns 82 ks effective exposure time for the XIS0/1/3 detectors. Since the vignetting effect was not accounted for by the `xisexpmapgen` task, we generated a vignetting map using `XISSIM`, simulating the vignetting effect by inputting a flat-field image. Subsequently, we multiplied the exposure map by the normalized vignetting map to generate the effective exposure time map[6] and divided the counts map by it to generate the count rate map.

Table 2
Spectral Extraction Regions

	a222-1	a222-2	a223-1	a223-2	fila-box	bkg
Radius [arcmin]	0–3	3–8.5	0–3	3–7.8	6.1 × 5.3	
Area [arcmin^2]	28.24	90.57	22.47	39.54	32.73	26.90

[5] https://darts.isas.jaxa.jp/astro/suzaku/analysis/process/v2changes/criteria-xis.html
[6] https://heasarc.gsfc.nasa.gov/docs/suzaku/analysis/expomap.html

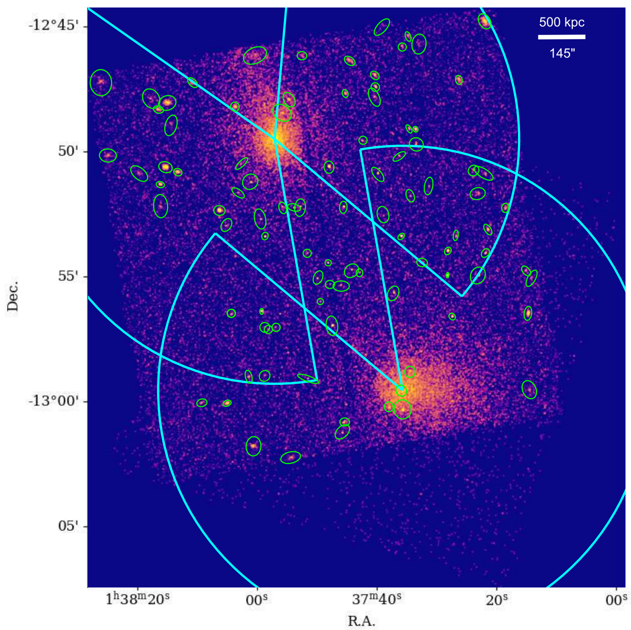

Figure 2. The Chandra image of A222/223 in the 0.5–7.0 keV band. The cyan sectors indicate the regions from which surface brightness profiles were extracted, while the green circles denote the exclusion zones for point sources. The image was smoothed using a Gaussian kernel with a width of 1.35".

2.2. *Effects of Scattered Light*

Because the primary objective of this work is to detect excess emission in the filament region, which is expected to be very faint (if any at all), we must carefully assess all sources of contamination. For Suzaku observations, scattered light is a major issue (Ishisaki et al. 2007). We utilized data from Chandra, making use of its superior angular resolution, and the XISSIM simulator to compute scattered light distributions.

We used Chandra Interactive Analysis of Observations (CIAO) v4.15 and CALDB 4.11.2[7] to process the Chandra data. The event and auxiliary files were generated using the chandra-repro task, and all observations were merged. Stowed event files were used as particle background. The image is shown in Figure 2. To derive cluster surface brightness profiles, we defined regions (in cyan) that avoid the filament region and the A223 subcluster (see Appendix). The point sources detected (with wavdetect) are shown in green ellipses and are excluded from subsequent analyses. The surface brightness profiles (in the 0.5–7 keV band) are shown in Figure 3 for A222 and A223, respectively.

The surface brightness profiles of the clusters were fitted with a double beta model by pyproffit (Eckert et al. 2020):

$$I(r) = I_0[(1 + (x/r_{c,1})^2)^{-3\beta+0.5} + R(1 + (x/r_{c,2})^2)^{-3\beta+0.5}] + B, \quad (1)$$

where x is radial distance, and B represents the sky background. The best fits are shown in Figure 3, with the χ^2 values being 54 (39 dof) and 45 (39 dof) for A222 and A223, respectively, and the model parameters summarized in Table 3. The best-fit surface brightness profiles were used to generate input images for the XISSIM simulator, and the results are shown in Figure 4. For the simulation, we adopted an absorbed APEC spectral model, with a temperature of 3 keV, which is typical of galaxy clusters of $M_{\rm tot} \sim 3 \times 10^{14} M_\odot$ (Finoguenov et al. 2001; Dietrich et al. 2012). We ran the simulation to collect 10^6 photons for XIS0, XIS1, and XIS3, respectively.

The output images from the simulation are shown in Figure 5, which shows the distribution of scattered X-rays from each of the regions of interest. Based on the images, we computed the fraction of the flux of a "source" region that is scattered to all the other "receiving" regions, and the results are summarized in Table 4. Clearly, the effects of scattered light are significant for all regions and must, therefore, be taken into account properly in subsequent analyses.

3. Results

A spectrum was extracted from each of the regions of interest, as well as the sky background region. It contains contributions from the non-X-ray background (NXB), the cosmic X-ray background (CXB), the Local Bubble (LHB), and possibly the Galactic halo (GH), which need to be carefully modeled, in order to reveal signals of scientific interest:

1. *Non-X-ray background.* The NXB spectrum was generated with the xisnxbgen task. Because the counts in the 10–14 keV band are dominated by NXB, we use them to scale the NXB spectrum. The uncertainties are estimated to be around 3.6% (Tawa et al. 2008).
2. *Cosmic X-ray background.* The log N–log S function of AGN derived from the Chandra Deep Field South (CDF-S) survey was used to estimate the unresolved CXB contribution (Lehmer et al. 2012). Here, we focused on the 2.0–8.0 keV band and computed the CXB surface brightness with the cxbtools tool (De Plaa 2017). For spectral analyses, we adopted an absorbed power law to model CXB, with the photon index fixed at 1.41. We also computed uncertainties for the regions of interest, as shown in Table 5, and considered three cases: CXB at the mean level (1.26×10^{-11} erg s^{-1} cm^{-2} deg^{-2}, referred to as "med" hereafter), 1σ higher ("hi"), and 1σ lower ("lo").
3. *The Local Bubble and Galactic Halo.* To constrain the LHB and possible GH contributions, we included the ROSAT All-Sky Survey (RASS) data (Snowden et al. 1997) in the fitting. We extracted an RASS spectrum from an annulus centered at the midpoint along the merger axis of the two clusters, with inner and outer radii

[7] https://cxc.cfa.harvard.edu/ciao/

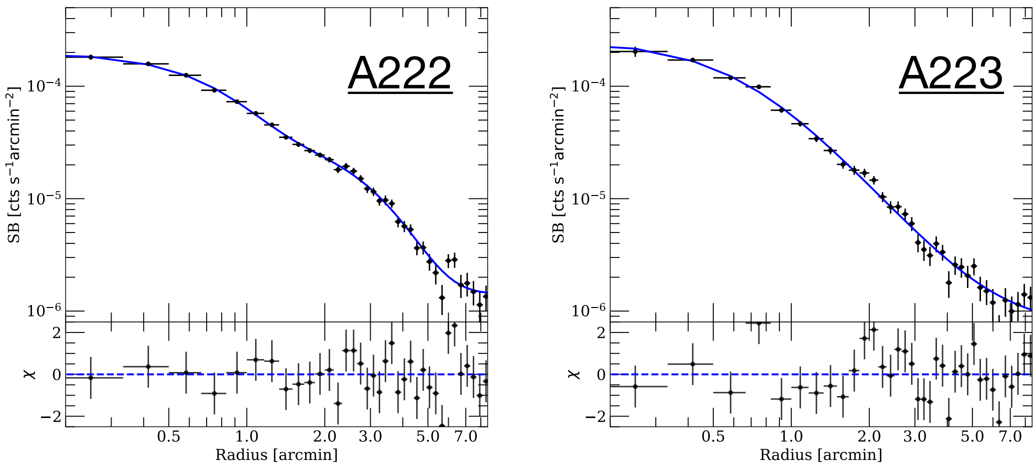

Figure 3. The surface brightness profile of A222 (left) and A223 (right). The data were logarithmically rebinned, with the non-X-ray background subtracted. The best-fit double beta models (see the main text) are shown in solid lines. The residuals are shown in the bottom panels.

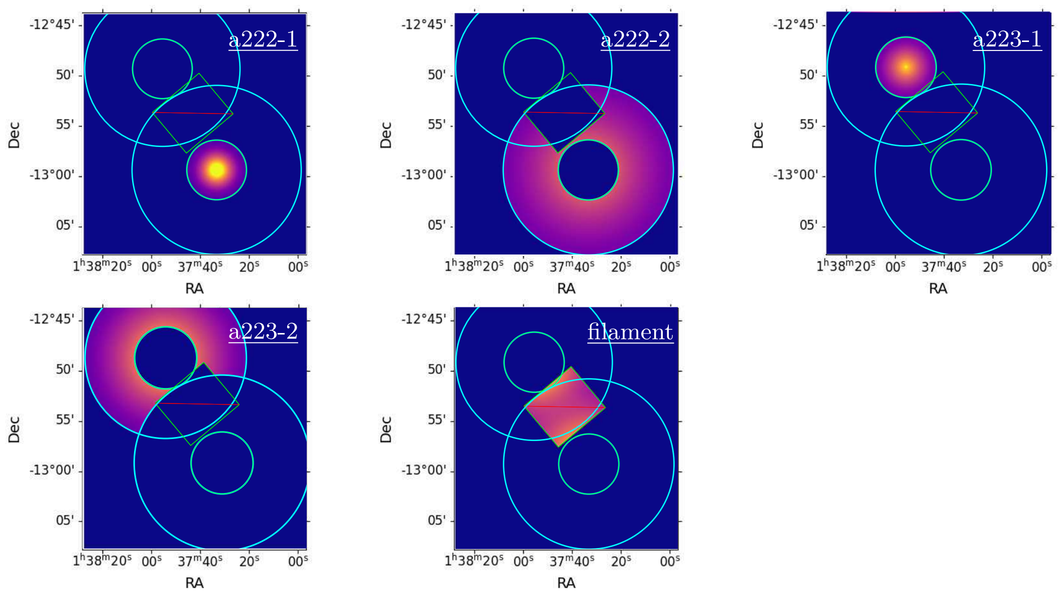

Figure 4. Input images to the *XISSIM* simulation for the regions shown in the rows of Table 4. The surface brightness distributions were derived from the Chandra surface brightness profiles.

Table 3
Best-fit Parameters of the Double Beta Model

Cluster	β	$r_{c,1}$	$r_{c,2}$	R	$\log_{10} I_0$	$\log_{10} B$
A222	0.47 ± 0.02	0.00 ± 0.05	0.56 ± 0.04	1.07 ± 0.15	−3.67 ± 0.06	−5.78 ± 0.12
A223	0.59 ± 0.02	0.13 ± 0.04	0.65 ± 0.06	0.91 ± 0.20	−3.54 ± 0.08	−6.56 ± 0.30

Note. $r_{c,1}$ and $r_{c,2}$ are in units of arcmin. I_0 and B are in units of cts s^{-1} arcmin^{-2}.

of 1° and 2°, respectively. We modeled the spectrum with an APEC (for LHB), an absorbed APEC (for GH) and a power law (for CXB), with chemical abundances fixed to $1Z_\odot$. While the preliminary temperature of LHB and GH were set to be 0.08 keV and 0.2 keV, the best-fit LHB temperature and GH temperature were found at 0.092 ± 0.012 keV and 0.196 ± 0.007 keV, which are in line with previous results (Kuntz & Snowden 2000;

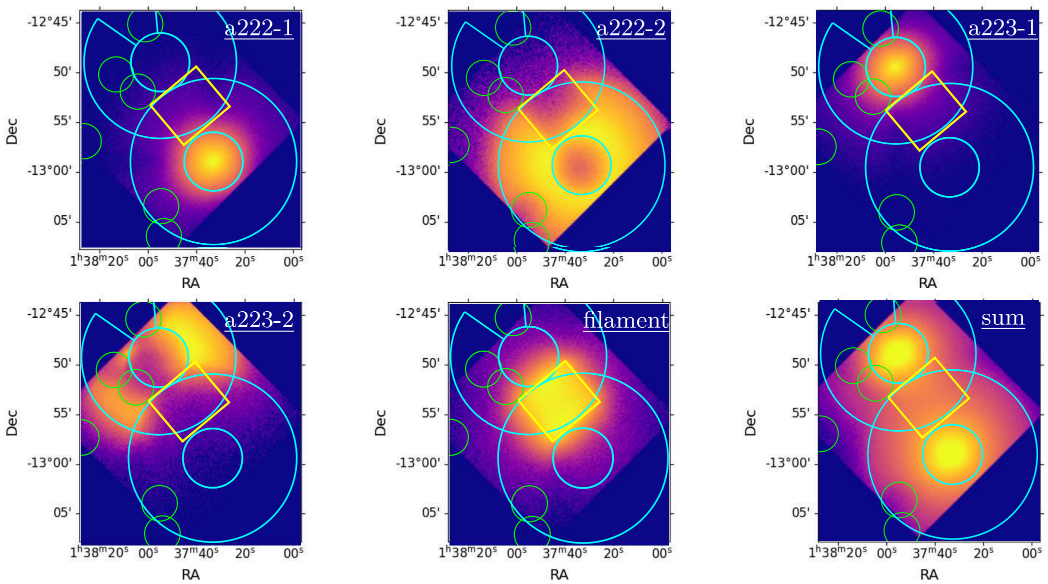

Figure 5. Simulated distribution of scattered emission. The distribution is shown for each of the regions of interest. The bottom-right panel shows the sum of all.

Table 4
Scattered Flux Fraction (%)

Source Region → Receiving Region ↓	a222-1	a222-2	a223-1	a223-2	Filament
a222-1	84.61	13.21	0.10	0.08	2.77
a222-2	12.50	80.73	0.70	3.47	12.41
a223-1	0.10	0.10	90.64	15.29	7.02
a223-2	0.13	0.76	4.62	75.05	3.55
filament	2.48	2.97	3.72	3.59	73.93
bkg	0.18	2.23	0.2	2.52	0.32

Note. Shown is the fraction of the flux of a source region (as in Figure 4) that is scattered to a "receiving" region or that of the remaining flux in the source region. Also see Figure 5.

Table 5
1σ Uncertainties of Unresolved CXB Fluxes

a222-1	a222-2	a223-1	a223-2	fila-box	bkg
2.68	1.39	2.75	2.17	2.39	2.64

Note. In units of 10^{-12} erg s^{-1} cm^{-2} deg^{-2}, computed in the 2–8 keV band.

Yeung et al. 2024 for LHB, and Henley & Shelton 2013; Yoshino et al. 2009 for GH).

4. *Scattered light.* All regions of interest are affected by scattered light. For spectral analyses, we used an APEC to model such a component for each region, with the model parameters tied together for all regions. The normalizations of the model are properly scaled to follow the ratios shown in Table 4. For instance, the ratio of the scattered flux in a222-2 to the flux in a222-1 was determined by $\frac{12.50\,/\,A_{2-2}}{84.61\,/\,A_{2-1}}$, where A_{2-1} and A_{2-2} represent the sky areas of a222-1 and a222-2, respectively.

The above components are all subject to interstellar absorption in the Milky Way, except for LHB. We adopted the TBabs model for the absorption, with $N_{\rm Htot}$ fixed at $1.62 \times 10^{20}\,{\rm cm}^{-2}$, which is a weighted average based on the Swift survey[8] (Willingale et al. 2013). The spectra extracted from the a223-2 and bkg regions show an absorption line feature roughly at 0.65 keV. It appears in the XIS1 spectrum but not in the XIS0/3 spectra; it is likely an artifact caused by the Optical Blocking Filter (OBF) contamination in XIS1.[9] In subsequent spectral analyses, we simply excluded the feature (0.55–0.80 keV) from the XIS1 spectra.

With the spectra optimally binned (Kaastra & Bleeker 2016), we carried out joint spectral fits across all the regions (see Figure 1), as well as different instruments, to disentangle the source and background/foreground components. The best-fit model parameters are shown in Table 6 for the background/foreground components. The uncertainties were derived from MCMC analysis.

Figure 6 displays the spectra and corresponding best-fit model for the regions of interest. In the cluster outskirt regions (a222-2 and a223-2), CXB contributes most to the X-ray emission, followed by the intrinsic cluster emission and the scattered cluster light from the cores. The best-fit model parameters are shown in Table 7. The first set of uncertainties are the statistical errors derived from the MCMC analysis, while the second set are the systematic errors associated with the uncertainties in

8 https://www.swift.ac.uk/analysis/nhtot/docs.php
9 http://heasarc.nasa.gov/docs/suzaku/analysis/abc/

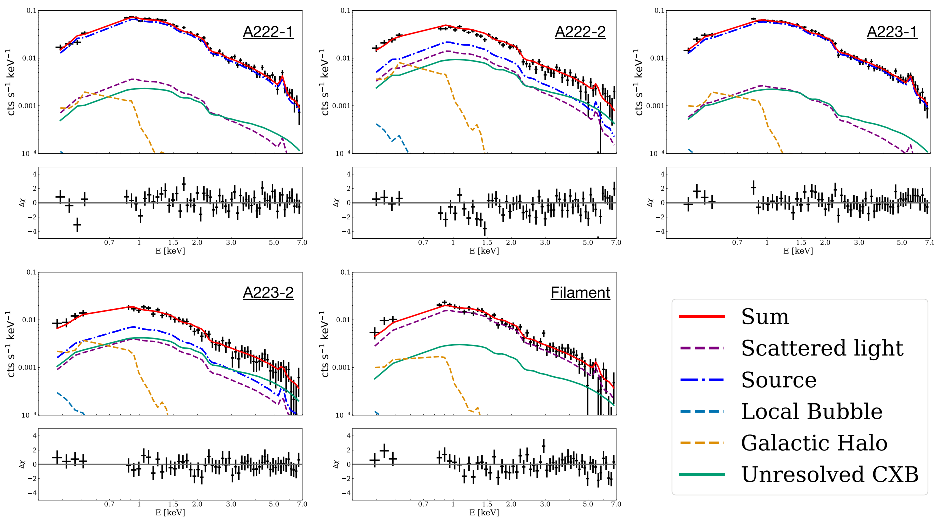

Figure 6. Observed X-ray spectra extracted from the regions of interest on XIS1 (see Figure 1). Also shown in solid lines are the best-fit models, along with various model components.

Table 6
Parameters of the Sky Background Model

Component	Model	Parameter	Value	Unit	Status
Relative normalization	Const	RASS	$1/400\pi$	…	Fixed
	…	XIS0	1	…	Fixed
	…	XIS1/3	1.0 ± 0.1	…	Free
Galactic absorption	TBabs	$N_{\rm H}$	1.62×10^{20}	cm^{-2}	Fixed
LHB	APEC	temperature	0.092 ± 0.012	keV	Free
	…	redshift	0	…	Fixed
	…	abundance	1	$Z_\odot$	Fixed
	…	norm	$5.39 \pm 0.16 \times 10^{-4}$	…	Free
GH	TBabs × APEC	temperature	0.191 ± 0.007	keV	Free
	…	redshift	0	…	Fixed
	…	abundance	1	$Z_\odot$	Fixed
	…	norm	$1.46 \pm 0.06 \times 10^{-3}$	…	Free
Unresolved CXB	TBabs × Powerlaw	pho index	1.41	keV	Fixed
	…	norm	[lo/med/hi]	…	Fixed

Note. Norm is a dimensionless value defined as $\frac{10^{-14}}{4\pi[D_A(1+z)]^2}\int n_e n_{\rm H} dV$ (https://heasarc.gsfc.nasa.gov/xanadu/xspec/manual/node134.html), where D_A is the angular diameter distance to the source (cm), dV is the volume element (cm^3), and n_e, $n_{\rm H}$ are the electron and H densities (cm^{-3}). The relative normalization reflects the difference in the spectral extraction area between RASS and Suzaku. $Z_\odot$ is the solar abundance using table Asplund et al. (2009).

determining CXB contributions (which were derived by comparing fits in "lo," "mid," and "hi" cases). The temperature is lower in the outskirts than in the core for A223, while it is comparable for A222, showing non-cool-core characteristics, which is consistent with previous findings from XMM-Newton (Durret et al. 2010). The metallicity in the cores is found to be around $0.3\,Z_\odot$, which is typical for galaxy clusters (Walker et al. 2019), while it is poorly constrained in the outskirts (and thus fixed to $0.3\,Z_\odot$, marked as 0.3^* in the fitting process). For the filament region, the observed spectrum is well modeled by summing the background/foreground components, indicating that the data do not require a WHIM contribution.

To derive upper limits on the properties of (undetected) WHIM emission, we refitted the spectra, with a new APEC component added to the model, while fixing the metallicities, the temperatures of GH and LHB, and the instrumental constants. We then carried out an MCMC analysis to determine confidence intervals for the remaining parameters,

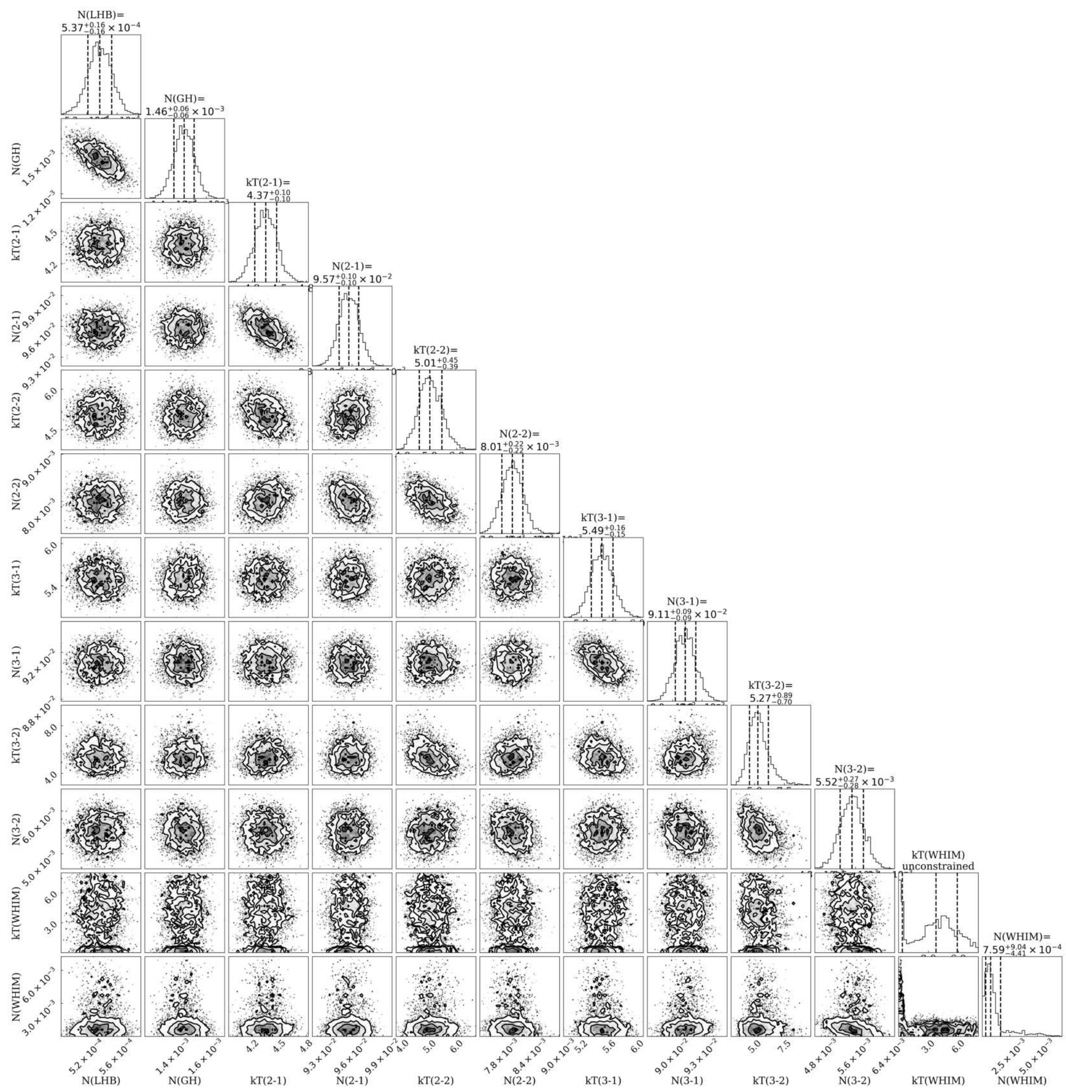

Figure 7. The parameter confidence intervals derived from MCMC analysis. APEC is adopted to model the emission from hot gas in all regions of interest. In the name of a parameter, "*N*" stands for normalization and "*kT*" stands for temperature, with the numbers indicating the region of interest. For example, *kT*(2–1) shows the temperature of hot gas in region a222-1. The line plots on the top show the distributions of the parameters, with 1σ confidence intervals indicated. kT is in units of keV, and normalization is dimensionless, as defined in Table 6.

Table 7
Best-fit Gas Properties in the Cluster Sectors

	a222-1	a222-2	a223-1	a223-2
Temperature (keV)	$4.37^{+0.10}_{-0.09}\ ^{+0.01}_{-0.08}$	$5.01^{+0.45}_{-0.39}\ ^{+0.59}_{-0.12}$	$5.49^{+0.18}_{-0.15}\ ^{+0.10}_{-0.26}$	$5.27^{+0.89}_{-0.70}\ ^{+0.07}_{-0.24}$
Abundance (solar)	$0.30^{+0.02}_{-0.02}\ ^{+0.08}_{-0.02}$	0.3 (fixed)	$0.42^{+0.07}_{-0.07}\ ^{+0.03}_{-0.02}$	0.3 (fixed)
Normalization (10^{-3})	$95.73^{+0.93}_{-0.91}\ ^{+3.96}_{-3.60}$	$8.01^{+0.23}_{-0.22}\ ^{+3.08}_{-2.53}$	$91.12^{+0.92}_{-0.90}\ ^{+1.97}_{-6.24}$	$5.52^{+0.26}_{-0.27}\ ^{+4.23}_{-3.44}$
C-statistics (dof)	67(61)	48 (54)	68 (75)	56 (68)

Note. Both statistical and systematic errors are shown (see the main text). The area-scaled normalization.

and the results are shown in Figure 7. The temperature of the WHIM component is poorly constrained. The best-fit normalization is 7.59×10^{-4}, although it is less than 2σ from 0. If we fixed the normalization at 3.5×10^{-3} (as in Werner et al. 2008), we derived an upper limit on temperature to be 2.34 keV (90% confidence). On the other hand, if we fixed the temperature at 0.91 keV (as in Werner et al. 2008), we found the upper limit on the normalization to be 1.29×10^{-3}, corresponding to a density of $1.32 \times 10^{-5}\,\mathrm{cm}^{-3}$ ($\rho/\rho_c \sim 60$) (we followed Werner et al. 2008 in converting normalization to density).

4. Discussion

Motivated by the detection of X-ray emission from a filament that connects A222 and A223 (Werner et al. 2008), we conducted a detailed study of the system with data from the Suzaku observations. The initial intention was to take advantage of the low NXB of the Suzaku detectors for detecting the extended emission of low surface brightness. However, we quickly ran into scattered light issues, which add comparable uncertainties in determining surface brightness as the CXB. The results show that the emission detected in the said WHIM region (Werner et al. 2008) can be accounted for (within uncertainties) by the combination of the scattered cluster emission, CXB, Galactic foreground, and NXB. A WHIM component can be accommodated by the data, but its properties are not well constrained. With one parameter (normalization or temperature) fixed at the value in Werner et al. (2008), the 90% confidence upper limit on the other parameter is consistent with the published results.

A possible way to reduce the CXB flux uncertainties in a Suzaku observation is to lower the source detection limit by also using data from observations with the telescopes of better angular resolution (e.g., Bulbul et al. 2016; Zhang et al. 2020). To this end, we attempted to improve the constraints on the WHIM emission with the XMM-Newton data. The details of the data reduction are shown in the Appendix. In the end, we reduced the CXB flux and its uncertainty by approximately 30%. We carried out similar spectral analyses to constrain the WHIM emission. The derived properties of cluster emission are consistent with those shown in Table A3, but those of the WHIM component are again poorly constrained. Fixing the WHIM temperature at $kT = 0.91$ keV, the upper limit on normalization is now 3.3×10^{-4}, corresponding to $3.4 \times 10^{-6}\,\mathrm{cm}^{-3}$; fixing the normalization at 3.5×10^{-3}, the upper limit on kT is 0.16 keV. Both of these upper limits are significantly lower than before.

In summary, based on the Suzaku observation alone, we can neither confirm nor rule out the presence of the WHIM emission, but the derived upper limits on the WHIM properties are broadly in line with the published results (Werner et al. 2008). Mirakhor et al. (2022) also found evidence for X-ray emission from a filament that connects A2029 and A2033, using Suzaku data, and determined the WHIM temperature to be $1.4^{+0.7}_{-0.5}$ keV, which is higher than our upper limit (derived with the help of XMM-Newton data). Even higher temperatures ($\gtrsim$3.5 keV) have been reported of WHIM emission in A399/401 and A3395/3391 (Sakelliou & Ponman 2004; Alvarez et al. 2018; Reiprich et al. 2021), based on *eROSITA*, which were attributed to shock heating in those systems. The APEC normalization of the WHIM component (derived with both kT and normalization free) implies a 90% upper limit of 101 on the WHIM overdensity, which aligns with previous results. The WHIM overdensity was determined to be $\rho/\rho_c \lesssim 60$ for A2801/2804/2811, (Sato et al. 2010) and $\sim$160 $\pm$ 70 (showing 90% confidence interval) for A2029/2033 (Mirakhor et al. 2022).

Acknowledgments

The authors thank the anonymous referee for their comments that have improved this paper. The authors wish to thank Jelle de Plaa, Jelle Kaastra, Chen Li, Zhenlin Zhu, Anwesh Majumder, Xiaoyuan Zhang, Dimitris Chatzigiannakis, Thomas Plsek, Jean-Paul Breuer, Jiejia Liu, Yu Zhou, Hiroki Akamatsu, Thomas Reiprich, Nobert Werner, Dominique Eckert, Junjie Mao, and Joop Schaye for helpful discussion, and the Tsinghua Astrophysics High-Performance Computing platform for providing computational and data storage resources. This work was supported in part by the National Natural Science Foundation of China through Grant 11821303, and by the Ministry of Science and Technology of China through Grant 2018YFA0404502. Y.L.C. acknowledges support from the China Scholarship Council, and DH acknowledges the financial support of the GAČR EXPRO grant No. 21-13491X. This research is based on observations obtained from the Suzaku satellite, a collaborative mission between the space agencies of Japan (JAXA) and the USA (NASA). This paper employs a list of Chandra data sets, obtained by the Chandra X-ray Observatory, contained in the Chandra Data Collection (CDC) DOI: 10.25574/cdc.371.

Appendix
Deriving Unresolved CXB Flux with XMM-Newton Observations

In previous study using Suzaku data, a uniform detection limit has been applied across the entire FOV (e.g., Walker et al. 2012; Bulbul et al. 2016). However, this approach does not utilize all the resolved CXB information. To address this, we calculated the unresolved point source flux on a pixel-by-pixel basis using the XMM-Newton sensitivity map. We followed the method outlined in H. R. Huang et al. (2025, in preparation) to generate a sensitivity map in the 2.0–4.5 keV band to determine the detection limit for each pixel in the XMM-Newton data. We integrated the CXB in every pixel using logN-logS relation of CDF-S from zeros to the detection limit of every pixel. The CDF-S logN-logS aligns with A222-223 FOV (see Figure A1).

To calculate the CXB resolved by XMM-Newton, we considered the scattering effects of point sources. First, we selected sources from the XMM-Newton catalog and ran `XISSIM` simulations for each source, all with the same input photon number. Then we used a calibrated on-axis source to

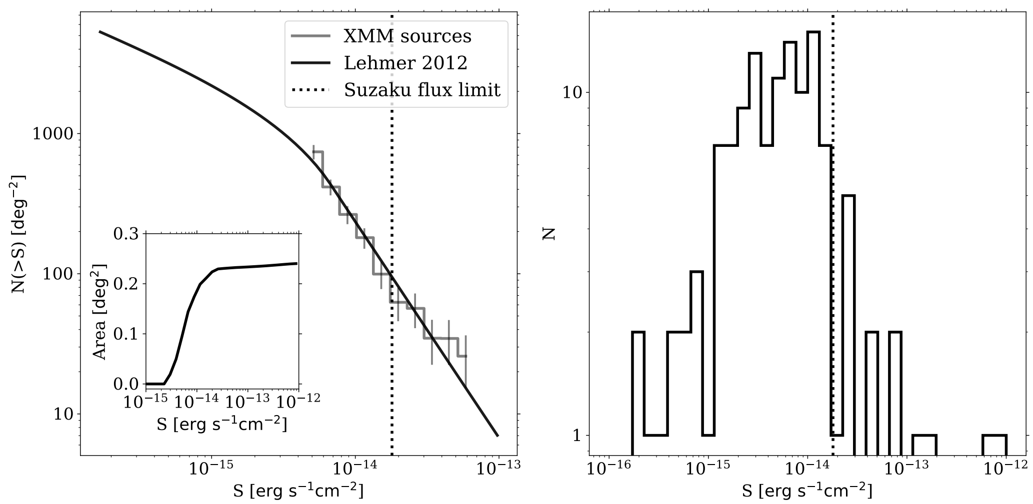

Figure A1. Left: The log *N*–log *S* curve of the XMM-Newton, the gray line is number of point sources whose fluxes higher than *x*-axis flux, corrected for the effective area. The black curve is the log *N*–log *S* curve from Lehmer et al. (2012). Right: The histogram of point sources. The dotted line is the Suzaku detection limit.

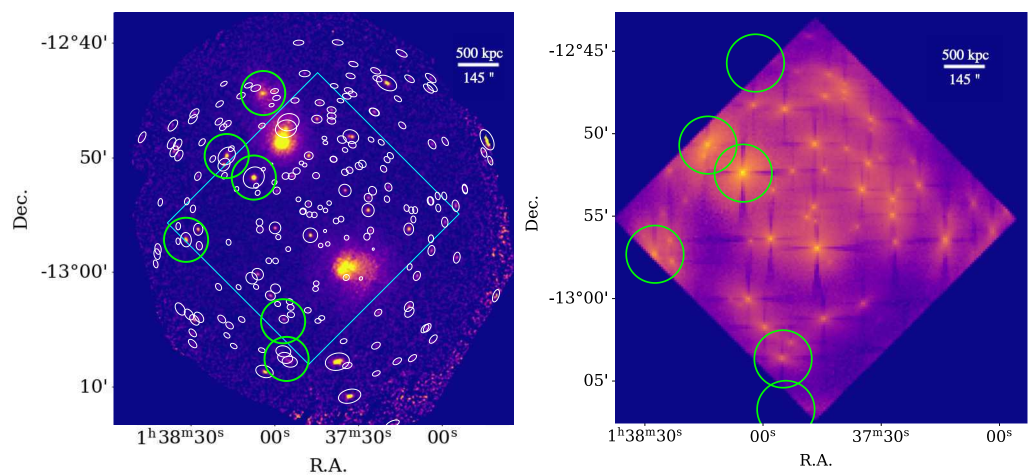

Figure A2. Left: The 0.5–7.0 keV mosaic image from XMM-Newton, smoothed by a Gaussian kernel of FWHM 10″. White ellipses are the point sources resolved by XMM-Newton. Green circles are the point source exclusion regions for Suzaku. Right: The output XISSIM map of XMM-Newton resolved point sources in XIS1 in the 0.5–12.0 keV band.

account for vignetting effect, and scale output image with source fluxes in XMM-Newton catalog. Lastly, we summed all the output images, which were then used in subsequent analyses. In Figure A2, the resolved point sources are marked in XMM-Newton image (white). In the XMM-Newton image, we can see the northeastern subcluster associated with A223 is visible in both XMM-Newton, but is undetected in the Suzaku observations due to the limited FOV. The centroid of this subcluster is located at a projected angular separation of $4\farcm8$ from the A223 cluster center, corresponding to a physical separation of approximately 987 kpc, which is positioned at (01:38:01.8, −12:45:07.0) (Dietrich et al. 2002). Separating the subcluster from the main cluster is difficult, so the subcluster mass was not measured in previous works (Dietrich et al. 2002, 2005). The mass density map from weak lensing analysis is available in Dietrich et al. (2012).

Using the updated CXB tables of resolved (Table A1) and unresolved CXB (Table A2), we refitted the spectra. The CXB resolved by XMM-Newton was additionally modeled by a power law. The photon index is constrained at 1.89 ± 0.34 by fitting XMM-Newton sky background spectra. We considered the photon index uncertainties, and the normalization is ensured to be the same. Table A3 shows the spectral fitting results. The properties are in line with the results in Section 3 in 1σ.

Table A1
Unresolved CXB Fluxes and the 1σ Errors

a222-1	a222-2	a223-1	a223-2	fila-box	bkg
9.14 ± 1.42	7.68 ± 0.63	7.52 ± 1.24	8.06 ± 0.95	7.25 ± 0.83	8.37 ± 1.24

Note. The flux is in the 2.0–8.0 keV band. The flux unit is 10^{-12} erg s^{-1} cm^{-2} deg^{-2}.

Table A2
Resolved CXB Flux and the 1σ Errors

a222-1	a222-2	a223-1	a223-2	fila-box	bkg
0.84 ± 0.14	2.22 ± 0.37	3.25 ± 0.54	2.85 ± 0.47	4.41 ± 0.73	0.15 ± 0.03

Note. The photon index is 1.89. The flux is in the 2.0–8.0 keV band. The flux unit is 10^{-12} erg s^{-1} cm^{-2} deg^{-2}.

Table A3
Gas Properties of the Cluster Sectors

	a222-1	a222-2	a223-1	a223-2
Temperature (keV)	$4.46^{+0.11}_{-0.10}$ $^{+0.18}_{-0.06}$ $^{+0.21}_{-0.04}$	$5.89^{+0.85}_{-0.56}$ $^{+0.97}_{-0.03}$ $^{+1.68}_{-1.03}$	$5.70^{+0.19}_{-0.15}$ $^{+0.13}_{-0.18}$ $^{+0.15}_{-0.41}$	$6.40^{+1.26}_{-1.00}$ $^{+1.23}_{-0.52}$ $^{+1.90}_{-1.37}$
Abundance (solar)	$0.33^{+0.02}_{-0.02}$ $^{+0.02}_{-0.05}$ $^{+0.02}_{-0.03}$	0.3^{*}	$0.42^{+0.07}_{-0.07}$ $^{+0.01}_{-0.01}$ $^{+0.13}_{-0.03}$	0.3^{*}
Normalization (10^{-3})	$97.31^{+1.00}_{-1.10}$ $^{+7.45}_{-2.99}$ $^{+14.06}_{-7.32}$	$6.84^{+0.20}_{-0.22}$ $^{+1.41}_{-0.88}$ $^{+3.33}_{-2.18}$	$88.23^{+0.81}_{-0.80}$ $^{+3.56}_{-2.21}$ $^{+10.64}_{-9.48}$	$5.11^{+0.22}_{-0.21}$ $^{+1.40}_{-2.81}$ $^{+10.23}_{-4.88}$
C-statistics (dof)	65(60)	50(48)	45(60)	36(55)

Note. The first errors presented in the results are the statistical errors, the second errors represent the systematic errors of different unresolved CXB levels, and the third errors refer to the systematic errors of different photon indices of resolved CXB. The C-statistics here refer to the fitting statistics of XIS1 spectra.

References

Alvarez, G. E., Randall, S. W., Bourdin, H., Jones, C., & Holley-Bockelmann, K. 2018, ApJ, 858, 44
Asplund, M., Grevesse, N., Sauval, A. J., & Scott, P. 2009, ARA&A, 47, 481
Bulbul, E., Randall, S. W., Bayliss, M., et al. 2016, ApJ, 818, 131
Cen, R., & Fang, T. 2006, ApJ, 650, 573
Cen, R., & Ostriker, J. P. 1999, ApJ, 514, 1
Davé, R., Cen, R., Ostriker, J. P., et al. 2001, ApJ, 552, 473
De Plaa, J., 2017 CXBTools, Zenodo
Dietrich, J. P., Clowe, D. I., & Soucail, G. 2002, A&A, 394, 395
Dietrich, J. P., Schneider, P., Clowe, D., Romano-Díaz, E., & Kerp, J. 2005, A&A, 440, 453
Dietrich, J. P., Werner, N., Clowe, D., et al. 2012, Natur, 487, 202
Durret, F., Laganá, T. F., Adami, C., & Bertin, E. 2010, A&A, 517, A94
Eckert, D., Finoguenov, A., Ghirardini, V., et al. 2020, OJAp, 3, 12
Fang, T., Mathur, S., & Nicastro, F. 2024, Handbook of X-Ray and Gamma-Ray Astrophysics (Singapore: Springer Nature), 4851
Finoguenov, A., Reiprich, T. H., & Böhringer, H. 2001, A&A, 368, 749
Henley, D. B., & Shelton, R. L. 2013, ApJ, 773, 92
Ishisaki, Y., Maeda, Y., Fujimoto, R., et al. 2007, PASJ, 59, S113
Kaastra, J. S., & Bleeker, J. A. M. 2016, A&A, 587, A151
Kuntz, K. D., & Snowden, S. L. 2000, ApJ, 543, 195
Lehmer, B. D., Xue, Y. Q., Brandt, W. N., et al. 2012, ApJ, 752, 46
Mirakhor, M. S., Walker, S. A., & Runge, J. 2022, MNRAS, 509, 1109
Reiprich, T. H., Veronica, A., Pacaud, F., et al. 2021, A&A, 647, A2
Sakelliou, I., & Ponman, T. J. 2004, MNRAS, 351, 1439
Sato, K., Kelley, R. L., Takei, Y., et al. 2010, PASJ, 62, 1423
Shull, J. M., Smith, B. D., & Danforth, C. W. 2012, ApJ, 759, 23
Snowden, S. L., Egger, R., Freyberg, M. J., et al. 1997, ApJ, 485, 125
Tawa, N., Hayashida, K., Nagai, M., et al. 2008, PASJ, 60, S11
Tuominen, T., Nevalainen, J., Tempel, E., et al. 2021, A&A, 646, A156
Walker, S., Simionescu, A., Nagai, D., et al. 2019, SSRv, 215, 7
Walker, S. A., Fabian, A. C., Sanders, J. S., George, M. R., & Tawara, Y. 2012, MNRAS, 422, 3503
Werner, N., Finoguenov, A., Kaastra, J. S., et al. 2008, A&A, 482, L29
Willingale, R., Starling, R. L. C., Beardmore, A. P., Tanvir, N. R., & O'Brien, P. T. 2013, MNRAS, 431, 394
Yeung, M. C. H., Ponti, G., Freyberg, M. J., et al. 2024, A&A, 690, A399
Yoshino, T., Mitsuda, K., Yamasaki, N. Y., et al. 2009, PASJ, 61, 805
Zhang, X., Simionescu, A., Akamatsu, H., et al. 2020, A&A, 642, A89